Scattering of TE Waves from a Cylindrical Scatterer Buried Inside a Two Layer Lossy Earth with Sinusoidal Air-Earth Interface

C. N. Vazouras[a] , P. G. Cottis[b] and J. D. Kanellopoulos[b]

[a] Hellenic Naval Academy, Hatzikyriakou Ave., Piraeus 18539, Greece.
[b] School of Electrical and Computer Engineering, National Technical University of Athens, Iroon Polytechniou 9, Athens 15773, Greece.

Abstract. Scattering from metallic and penetrable objects buried inside the ground is of interest for remote sensing applications. In this work, a cylindrical scatterer buried inside a two-layer lossy ground with a sinusoidal air-earth interface is considered, with an incident field impinging from the air region. Thus, a realistic ground model, with a surface layer of increased conductivity, is incorporated. The sinusoidal profile adopted to model the surface roughness is amenable to a semi-analytic (moment method) treatment of the scattered field. An integral equation approach combined with the extended boundary condition method has been employed for the formulation of the boundary value scattering problem. The Green function of the problem and the electric field in the absence of the scatterer are expressed in terms of Floquet spatial harmonics. The electric field inside the scatterer is expanded in terms of circular cylindrical wavefunctions and the expansion coefficients are computed by means of a moment method procedure. Subsequently, the far-zone scattered field is evaluated asymptotically by means of the steepest descent technique. Numerical results obtained show that the main factors affecting the scattered field are the conductivity of the ground and the horizontal position of the scatterer with respect to dips and lifts of the sinusoidal surface.

Keywords: electromagnetic scattering; underground cylinders; sinusoidal surface; surface layer.
PACS: 41.20.Jb

INTRODUCTION

Scattering from metallic or penetrable objects buried inside a lossy dielectric half-space, and the interaction between the scatterers and the surrounding media, has applications to remote sensing and geoscience [1 – 4] and various other fields as medical physics [5]. A considerable number of work has been carried out based on the assumption of a flat interface, while some recent studies incorporate a random rough surface profile (see e.g. [5, 6] and references therein) which may be addressed by analytical models (e.g. small perturbation approach) or numerical solutions combined with Mont Carlo averaging. In the present study, the assumption of a sinusoidal profile for the air-ground interface is combined with a two-layer model for the structure of the ground. This approach incorporates a more realistic model for the ground (as

1

compared with the simple homogeneous halfspace model used in previous literature), while taking into account both the surface roughness and the surface layer in a way that allows derivation of good qualitative results for various roughness scales at low numerical cost.

The geometry of the problem is depicted in Fig. 1, where the sinusoidal profile $\zeta(x)$ is characterized by the height h and the spatial period d as follows

$$\zeta(\mathrm{x}) = -\mathrm{h}\cos\left(2\pi\frac{\mathrm{x}}{\mathrm{d}}\right) \qquad (1)$$

The distances of the axis of the cylindrical scatterer from the xz- and the xy-plane are denoted by A and D, respectively, α is the cylinder radius and n_1, n_2, n_3 are the complex refractive indices of the two-layer ground and the scatterer, respectively. The surface layer has a thickness b with reference to the xy-plane. A TE plane incident wave impinges on the surface of the ground with its direction perpendicular to the axis of the cylinder, making an angle θ_i with respect to the vertical direction. The whole space is assumed magnetically homogeneous ($\mu = 4\pi\cdot10^{-7}$ H/m). A harmonic $exp(-j\omega t)$ time dependence is assumed and suppressed throughout the analysis.

FIGURE 1. Geometry of the scattering problem.

An integral equation approach is adopted for the formulation of the boundary value problem in conjunction with the Extended Boundary Condition (EBC) method. Green's theorem is applied to formulate the integral equation for the unknown electric field inside the scatterer.The Green function of the problem and the electric field in the absence of the scatterer are appropriately expanded in terms of Floquet spatial harmonics using the EBC method [7, 8]. The electric field inside the scatterer is expanded in terms of circular cylindrical wavefunctions and the integral equation is transformed to an infinite system of algebraic equations, which is truncated and solved for the unknown expansion coefficients of the internal electric field. Evaluation of the scattered far field in the air region is accomplished asymptotically by the steepest descent method. Finally, numerical results are obtained to estimate the impact of various parameters of

2

the problem and to investigate possible applications to remote sensing and underground mapping.

FORMULATION OF THE BOUNDARY VALUE PROBLEM

We assume a y-polarized unitary incident electric field $\vec{E}_i(\vec{r}) = \psi_i(\vec{r})\,\hat{y}$, with

$$\psi_i(\vec{r}) = \exp[j(k_0 \sin\theta_i\, x - k_0 \cos\theta_i\, z)] \tag{2}$$

where k_0 is the free-space wavenumber.

We denote by $\psi_0(\vec{r})$ and $\psi(\vec{r})$ the electric field in the absence of the scatterer and the total electric field, respectively, and by $G(\vec{r};\vec{r}')$ the electric type Green function of the problem. The Green function $G(\vec{r};\vec{r}')$ is also y-polarized and is determined as the response to a unit excitation parallel to the y-axis located inside the second layer (i.e., $z' < -b$), which satisfies the wave equation in two dimensions

$$\left[\nabla^2 + k^2(\vec{r})\right] G(\vec{r};\vec{r}') = -\delta(\vec{r} - \vec{r}') \tag{3}$$

where

$$\vec{r} = x\,\hat{x} + z\,\hat{z} \quad , \quad \vec{r}' = x'\,\hat{x} + z'\,\hat{z} \tag{4}$$

and

$$k(\vec{r}) = \begin{cases} k_0 = \omega(\mu_0\,\varepsilon_0)^{1/2} & , \quad z > \zeta(x) \\ k_1 = k_0(\varepsilon_1 + j\sigma_1/\omega\varepsilon_0)^{1/2} & , \quad -b < z < \zeta(x) \\ k_2 = k_0(\varepsilon_2 + j\sigma_2/\omega\varepsilon_0)^{1/2} & , \quad z < -b \end{cases} \tag{5}$$

is the wavenumber in each of the three layers shown in Fig. 1, while the wavenumber k_3 corresponding to the scatterer is defined analogously. The Green function $G(\vec{r};\vec{r}')$ must also satisfy the boundary conditions, i.e. continuity at the two interfaces $z = -b$ and $z = \zeta(x)$.

Applying Green's theorem, the following compact integral expression in two dimensions for the total field $\psi(\vec{r})$ in the presence of the scatterer is obtained

$$\psi(\vec{r}) = \psi_0(\vec{r}) + \left(k_3{}^2 - k_2{}^2\right) \iint\limits_{S_t} G(\vec{r};\vec{r}')\psi(\vec{r}')\,dS' \tag{6}$$

where S_t is the cross-section of the cylindrical scatterer and the observation point $\vec{r}$ can be in any region. If $\vec{r}$ is considered inside the region S_t, eq. (6) becomes an integral equation for the total electric field inside the scatterer. After solving the integral equation for the internal electric field, one can subsequently evaluate the total electric field via (6) by taking $\vec{r}$ in the region of interest.

The first step of the above procedure is to determine the total field $\psi_0(\vec{r})$ in the absence of the scatterer applying the EBC method. To this end, we assume a y-polarized plane wave, as given by (2), impinging from the air on the sinusoidal surface as shown in Fig. 1. Then, the total electric field can be written [7, 8] as an appropriate superposition of Floquet modes

$$\psi_0(\vec{r}) = \sum_{n=-\infty}^{+\infty} \frac{C_n^{(m)}}{\sqrt{k_{mzn}}} \exp\left[j\vec{k}_{mn}^{(-)} \cdot \vec{r}\right] + \sum_{n=-\infty}^{+\infty} \frac{D_n^{(m)}}{\sqrt{k_{mzn}}} \exp\left[j\vec{k}_{mn}^{(+)} \cdot \vec{r}\right] \tag{7}$$

where the upward or downward directed (corresponding to the supersripts $\pm$, respectively) wavevectors are given by

$$\vec{k}_{mn}^{(\pm)} = k_{xn}\,\hat{x} \pm k_{mzn}\,\hat{z} \quad , \quad m = 0, 1, 2 \tag{8}$$

and

$$k_{xn} = k_0 \sin\theta_i + \frac{2n\pi}{d} \quad , \quad k_{mzn} = \left(k_m^{\ 2} - k_{xn}^{\ 2}\right)^{1/2} \tag{9}$$

The indices *m = 0, 1, 2* correpond to the regions *z > h, − b < z < h* and *z < − b*, respectively, while the selvedge region *− h < z < h*, where a different situation arises, does not need to be considered in the present analysis. The square roots of k_{mzn} are defined with the appropriate branch cuts so that the radiation conditions hold

$$\mathrm{Re}\left(k_{mzn}\right) \geq 0 \quad , \quad \mathrm{Im}\left(k_{mzn}\right) \geq 0$$

The incident field from the air region, according to (2), corresponds to

$$C_n^{(0)} = \delta_{n0}\sqrt{k_{0zn}} \tag{10}$$

where δ_{n0} is the Kronecker delta coefficient. Due to the outgoing wave condition for the field in the lower region *z < − b*, the corresponding upward wave coefficients are identically zero

$$D_n^{(2)} = 0 \qquad \forall\, n \in \{-\infty, \dots, -1, 0, 1, \dots, +\infty\} \tag{11}$$

Applying the extended boundary conditions on the sinusoidal interface *z = ζ(x)*, the following matrix equations [7, 8] are obtained

$$\widetilde{C}^{(m)} = -\left[R_{Dm}^-\right]\widetilde{\beta}^s - \left[R_{Nm}^-\right]\widetilde{\alpha}^s \tag{12}$$

$$\widetilde{D}^{(m)} = -\left[R_{Dm}^+\right]\widetilde{\beta}^s - \left[R_{Nm}^+\right]\widetilde{\alpha}^s \tag{13}$$

where the tilde (~) denotes a column matrix as follows

$$\widetilde{C}^{(m)} = \begin{bmatrix} \dots \\ C_{-1}^{(m)} \\ C_0^{(m)} \\ C_1^{(m)} \\ \dots \end{bmatrix} \quad , \quad \widetilde{D}^{(m)} = \begin{bmatrix} \dots \\ D_{-1}^{(m)} \\ D_0^{(m)} \\ D_1^{(m)} \\ \dots \end{bmatrix} \quad , \quad \widetilde{\alpha}^s = \begin{bmatrix} \dots \\ \alpha_{-1}^s \\ \alpha_0^s \\ \alpha_1^s \\ \dots \end{bmatrix} \quad , \quad \widetilde{\beta}^s = \begin{bmatrix} \dots \\ \beta_{-1}^s \\ \beta_0^s \\ \beta_1^s \\ \dots \end{bmatrix}$$

The elements of the square matrices *[R]* involved in (12) and (13) are given in the Appendix and α_n^s, β_n^s are the Fourier expansion coefficients adopted for the field boundary values of ψ and $\partial\psi/\partial n$ on the sinusoidal interface. Imposing the boundary conditions at *z = − b* and taking (11) into account, the following equations are obtained

$$\widetilde{D}^{(1)} = [L_C]\widetilde{C}^{(1)} \tag{14}$$

$$\widetilde{C}^{(2)} = [M]\widetilde{C}^{(1)} \tag{15}$$

where [L_C] and [M] are diagonal matrices (corresponding to reflection and diffraction of Floquet waves on the *z = − b* plane) with elements given by

$$[L_C]_{nn} = R_n \exp(j2k_{1zn}b) \tag{16}$$

$$[M]_{nn} = T_n \exp\{j(k_{1zn} - k_{2zn})b\} \tag{17}$$

where

$$R_n = \frac{k_{1zn} - k_{2zn}}{k_{1zn} + k_{2zn}} \tag{18}$$

4

$$T_n = \frac{2\sqrt{k_{1zn}\,k_{2zn}}}{k_{1zn} + k_{2zn}} \tag{19}$$

Combining now (14) with (12)-(13), one obtains

$$\tilde{\beta}^s = -[S]\,\tilde{\alpha}^s \tag{20}$$

where

$$[S] = \left(\left[R_{D1}^+\right] - [L_C]\left[R_{D1}^-\right]\right)^{-1}\left(\left[R_{N1}^+\right] - [L_C]\left[R_{N1}^-\right]\right) \tag{21}$$

Substituting (20) into (12), α_n^s are obtained as

$$\tilde{\alpha}^s = \left(\left[R_{D0}^-\right][S] - \left[R_{N0}^-\right]\right)^{-1}\tilde{C}^{(0)} \tag{22}$$

The determination of α_n^s, β_n^s from (20)-(22) leads to the calculation of the column matrices $\tilde{C}^{(m)}$, $\tilde{D}^{(m)}$. The coefficients of interest for the present study are $C_n^{(2)}$ which, combining (12), (15), (20) and (22) are found to be

$$\tilde{C}^{(2)} = [M]\left(\left[R_{D1}^-\right][S] - \left[R_{N1}^-\right]\right)\left(\left[R_{D0}^-\right][S] - \left[R_{N0}^-\right]\right)^{-1}\tilde{C}^{(0)} \tag{23}$$

The Green function $G(\vec{r};\vec{r}')$ in the regions $z > h$ and $z < -b$ may be determined in a similar way. Since, for application of the integral equation (6), the source point is located in the lower layer, i.e. $z' < -b$, one may write

$$G(\vec{r};\vec{r}') = \begin{cases} G_{s,0}(\vec{r};\vec{r}') & , \quad z > h \\ G_{fs}(\vec{r};\vec{r}') + G_{s,2}(\vec{r};\vec{r}') & , \quad z < -b \end{cases} \tag{24}$$

where $G_{fs}(\vec{r};\vec{r}')$ is the "free space" Green function (corresponding to a homogeneous space with wavenumber k_2) and $G_{s,0}(\vec{r};\vec{r}')$, $G_{s,2}(\vec{r};\vec{r}')$ are the secondary fields induced in the corresponding regions. To apply the boundary conditions at $z = -b$ and $z = \zeta(x)$ we note that in both cases the relation $z > z'$ holds, and hence $G_{fs}(\vec{r};\vec{r}')$ may be written, according to the well known Weyl plane wave expansion, as

$$G_{fs}(\vec{r};\vec{r}') = T\left\{\frac{\exp[j\lambda x + j\upsilon_2(\lambda)z]}{\sqrt{\upsilon_2(\lambda)}}\right\} \tag{25}$$

where the operator T is defined as

$$T = \int_{-\infty}^{+\infty} d\lambda \, \frac{\exp[-j\lambda x' - j\upsilon_2(\lambda)z']}{\sqrt{\upsilon_2(\lambda)}} \tag{26}$$

and

$$\upsilon_2(\lambda) = \left(k_2^2 - \lambda^2\right)^{1/2} \qquad , \qquad \mathrm{Im}(\upsilon_2) \geq 0 \tag{27}$$

Since the operator T is linear and independent of x and z, the problem is simply reduced to that of determining the reflected field in the lower region $z < -b$ and the diffracted field in the upper region $z > h$ due to a plane wave

$$\psi_{\lambda,i}(\vec{r}) = \frac{\exp[j\lambda x + j\upsilon_2(\lambda)z]}{\sqrt{\upsilon_2(\lambda)}} \tag{28}$$

impinging from the lower region $z < -b$ on the plane interface $z = -b$. Then, the operator T is imposed to derive the full expressions for $G_{s,2}(\vec{r};\vec{r}')$ and $G_{s,0}(\vec{r};\vec{r}')$ which correspond to the

reflected and diffracted fields, respectively. The problem is strictly analogous to that of finding the field $\psi_0(\vec{r})$ in the absence of the scatterer and can be treated in the same way by substituting

$$k_0 \sin\theta_i \quad \leftrightarrow \quad \lambda \tag{29}$$

Thus, the waves associated with the incident field $\psi_{\lambda,i}(\vec{r})$ are expressed in a way analogous to (7)

$$\psi_\lambda(\vec{r}) = \sum_{n=-\infty}^{+\infty} \frac{A_n^{(m)}(\lambda)}{\sqrt{\upsilon_{mzn}}} \exp\left[j\vec{\upsilon}_{mn}^{(-)} \cdot \vec{r}\right] + \sum_{n=-\infty}^{+\infty} \frac{B_n^{(m)}(\lambda)}{\sqrt{\upsilon_{mzn}}} \exp\left[j\vec{\upsilon}_{mn}^{(+)} \cdot \vec{r}\right] \tag{30}$$

where

$$\vec{\upsilon}_{mn}^{(\pm)} = \upsilon_{xn}\,\hat{x} \pm \upsilon_{mzn}\,\hat{z} \quad , \quad m = 0, 1, 2 \tag{31}$$

with

$$\upsilon_{xn} = \lambda + \frac{2n\pi}{d} \quad , \quad \upsilon_{mzn} = \left(k_m^2 - \upsilon_{xn}^2\right)^{1/2} \quad , \quad \mathrm{Im}(\upsilon_{mzn}) \geq 0 \tag{32}$$

The symbol υ is used instead of k to emphasize the dependence of the corresponding wavenumbers on λ. The difference from the previous evaluation of $\psi_0(\vec{r})$ is that in the present case the incident wave comes form the lower region $z < -b$ instead of the upper region $z > h$. Thus, it should be set

$$B_n^{(2)}(\lambda) = B_n^{(2)} = \delta_{n0} \tag{33}$$

$$A_n^{(0)}(\lambda) = A_n^{(0)} = 0 \tag{34}$$

Application of the extended boundary condition for the sinusoidal profile $z = \zeta(x)$ yields the following matrix equations

$$\widetilde{A}^{(m)}(\lambda) = -\left[Q_{Dm}^-\right]\widetilde{\beta}_\lambda^s - \left[Q_{Nm}^-\right]\widetilde{\alpha}_\lambda^s \tag{35}$$

$$\widetilde{B}^{(m)}(\lambda) = -\left[Q_{Dm}^+\right]\widetilde{\beta}_\lambda^s - \left[Q_{Nm}^+\right]\widetilde{\alpha}_\lambda^s \tag{36}$$

where the coefficients $\alpha_{n,\lambda}^s, \beta_{n,\lambda}^s$ are directly analogous to α_n^s, β_n^s involved in the determination of the field $\psi_0(\vec{r})$. The matrices [Q] are obtained from the expressions of the corresponding matrices [R] (see the Appendix) by means of the substitution (29). On the other hand, application of the boundary conditions at $z = -b$ yields

$$\widetilde{B}^{(1)}(\lambda) = \left[L_{A,\lambda}\right]\widetilde{A}^{(1)}(\lambda) + \left[M_\lambda\right]\widetilde{B}^{(2)}(\lambda) \tag{37}$$

$$\widetilde{A}^{(2)}(\lambda) = \left[M_\lambda\right]\widetilde{A}^{(1)}(\lambda) - \left[L_{B,\lambda}\right]\widetilde{B}^{(2)}(\lambda) \tag{38}$$

where the matrices $[L_{A,\lambda}]$ and $[M_\lambda]$ are determined from $[L_C]$ and $[M]$, respectively, by the substitution (29), and $[L_{B,\lambda}]$ is diagonal with elements

$$\left[L_{B,\lambda}\right]_{nn} = R_{n,\lambda} \exp\left(-j2\upsilon_{2zn}b\right) \tag{39}$$

where

$$R_{n,\lambda} = \frac{\upsilon_{1zn} - \upsilon_{2zn}}{\upsilon_{1zn} + \upsilon_{2zn}} \tag{40}$$

Eliminating $\widetilde{\alpha}_\lambda^s$ and $\widetilde{\beta}_\lambda^s$, one finally obtains the following expressions for the coefficients of interest $A_n^{(2)}(\lambda)$ and $B_n^{(0)}(\lambda)$

6

$$\tilde{A}^{(2)}(\lambda) = [M_\lambda][S_A]([S_B] - [L_{A,\lambda}][S_A])^{-1}[M_\lambda]\tilde{B}^{(2)}(\lambda) - [L_{B,\lambda}]\tilde{B}^{(2)}(\lambda) \tag{41}$$

$$\tilde{B}^{(0)}(\lambda) = [S_0]([S_B] - [L_{A,\lambda}][S_A])^{-1}[M_\lambda]\tilde{B}^{(2)}(\lambda) \tag{42}$$

where

$$[S_A] = [Q_{D1}^-][Q_{D0}^-]^{-1}[Q_{N0}^-] - [Q_{N1}^-] \tag{43}$$

$$[S_B] = [Q_{D1}^+][Q_{D0}^-]^{-1}[Q_{N0}^-] - [Q_{N1}^+] \tag{44}$$

$$[S_0] = [Q_{D0}^+][Q_{D0}^-]^{-1}[Q_{N0}^+] - [Q_{N0}^+] \tag{45}$$

Having evaluated $A_n^{(2)}(\lambda)$ and $B_n^{(0)}(\lambda)$, one may impose the operator T to obtain the final expressions for $G_{s,2}(\vec{r};\vec{r}')$ and $G_{s,0}(\vec{r};\vec{r}')$

$$G_{s,2}(\vec{r};\vec{r}') = \int_{-\infty}^{+\infty} d\lambda \frac{\exp[-j\lambda x' - j\upsilon_2(\lambda)z']}{\sqrt{\upsilon_2(\lambda)}} \sum_{n=-\infty}^{+\infty} \frac{A_n^{(2)}(\lambda)}{\sqrt{\upsilon_{2zn}}} \exp[j\upsilon_{xn}x - j\upsilon_{2zn}z] \tag{46}$$

and

$$G_{s,0}(\vec{r};\vec{r}') = \int_{-\infty}^{+\infty} d\lambda \frac{\exp[-j\lambda x' - j\upsilon_2(\lambda)z']}{\sqrt{\upsilon_2(\lambda)}} \sum_{n=-\infty}^{+\infty} \frac{B_n^{(0)}(\lambda)}{\sqrt{\upsilon_{0zn}}} \exp[j\upsilon_{xn}x + j\upsilon_{0zn}z] \tag{47}$$

EVALUATION OF THE FAR FIELD IN THE AIR REGION

In the presence of a scatterer inside the second layer of the ground, the incident field is distorted due to the secondary field excited inside the scatterer. This field may be evaluated by properly expressing it as a superposition of scalar cylindrical wavefunctions

$$\psi(\vec{r}) = \sum_{m=-\infty}^{+\infty} E_m J_m(k_3\rho)e^{jm\varphi} \quad , \quad \vec{r} \in S_t \tag{48}$$

where the local polar coordinates (ρ, φ) are related to the initial coordinate system through

$$x = A + \rho\cos\varphi \quad , \quad z = -D + \rho\sin\varphi$$

At this point, one substitutes into the integral equation (6) the expressions (7) with $m = 2$ for the incident field, (46) for the secondary part of the Green function along with the well known eigenfunction expansion for the primary (free-space) part of the Green function, i.e.

$$G_{fs}(\vec{r};\vec{r}') = \frac{j}{4}H_0(k_2|\vec{r} - \vec{r}'|) = \frac{j}{4}\sum_{p=-\infty}^{+\infty} J_p(k_2\rho_<)H_p(k_2\rho_>)e^{jp(\varphi-\varphi')}$$

where

$$\rho_< = \min\{\rho,\rho'\} \quad , \quad \rho_> = \max\{\rho,\rho'\}$$

The standard procedure of multiplying by $exp(-js\varphi)$ (s is any integer), integrating over the cross-section of the cylindrical scatterer and making use of the orthogonal properties of the cylindrical basis functions over a period of 2π is then applied. Letting s vary over the whole set of integers, the following set of linear algebraic equations is obtained, whence the unknown expansion coefficients E_m may be evaluated.

$$j\pi K_s(k_2\alpha, k_3\alpha)E_s - j\sum_{m=-\infty}^{+\infty} K_{sm} L_m(k_2\alpha, k_3\alpha)E_m =$$

$$= 2(-1)^s \sum_{n=-\infty}^{+\infty} \frac{C_n^{(2)}}{\sqrt{k_{2zn}}} \exp\left[-js\tau_n + jk_{xn}A + jk_{2zn}D\right] \tag{49}$$

where

$$K_s(X, Y) = X H_{s+1}(X)J_s(Y) - Y J_{s+1}(Y)H_s(X) \tag{50}$$

$$L_m(X, Y) = Y J_{m+1}(Y)J_m(X) - X J_{m+1}(X)J_m(Y) \tag{51}$$

$$K_{sm} = j^{s-m} \sum_{n=-\infty}^{+\infty} e^{j2\pi nA/d} \int_{-\infty}^{+\infty} d\lambda \, \frac{A_n^{(2)}(\lambda)}{\sqrt{\mu_2 \, \upsilon_{2zn}}} \exp\left[j\upsilon_2(\lambda)D + j\upsilon_{2zn}(\lambda)D + js\Phi_n(\lambda) + jm\vartheta(\lambda)\right] \tag{52}$$

with

$$\tau_n = \sin^{-1}\left(\frac{k_{xn}}{k_2}\right) \tag{53}$$

$$\Phi_n(\lambda) = \tan^{-1}\left[\frac{\upsilon_{2zn}(\lambda)}{\upsilon_{xn}(\lambda)}\right] \tag{54}$$

$$\vartheta(\lambda) = \tan^{-1}\left[\frac{\upsilon_2(\lambda)}{\lambda}\right] \tag{55}$$

The matrix equation (49) can be truncated and solved numerically. In general, the truncation size concerning the series expansion of the Green function and the expansion of the incident field in terms of Floquet modes depends on the parameters k_1, k_2, h/d, k_0d; the truncation size concerning the expansion of the internal electric field depends mainly on $k_3\alpha$ and σ_3. As far as the convergence of the integrals K_{sm} is concerned, one may easily verify that it is quite fast, due to the factor $\exp\left[j\upsilon_2(\lambda)D + j\upsilon_{2zn}(\lambda)D\right]$ which decays exponentially with λ, while the rest of the integrand behaves as a power of λ, for large λ.

Having evaluated the expansion coefficients E_m, the scattered far field in the air region is determined through (6). To this end, the observation point $\vec{r}$ is taken in the region $z > h$ and all known quantities are inserted in (6). Employing the expression (47) for $G_{s,0}(\vec{r}; \vec{r}')$, the following expression for the electric field in the air region is obtained

$$\psi(\vec{r}) - \psi_0(\vec{r}) = \frac{j}{2}\sum_{m=-\infty}^{+\infty} E_m(-j)^m L_m(k_2\alpha, k_3\alpha) \sum_{n=-\infty}^{+\infty} \exp\left[j\frac{2\pi n}{d}A\right] I_n \tag{56}$$

where

$$I_n = \int_{-\infty}^{+\infty} d\lambda \, \frac{B_n^{(0)}(\lambda)}{\sqrt{\mu_2 \, \upsilon_{0zn}}} \exp\left[j\upsilon_2(\lambda)D - j\upsilon_{0zn}(\lambda)D + jm\vartheta(\lambda) + j\rho(\upsilon_{xn}\cos\varphi + \upsilon_{0zn}\sin\varphi)\right] \tag{57}$$

To evaluate the integrals I_n when $\rho \to +\infty$, the steepest descent method is applied. The final result for the scattered far field in the air region is obtained in the same way as in [2]

$$\psi(\vec{r}) - \psi_0(\vec{r}) = je^{-j\pi/4}\sqrt{\frac{\pi}{2k_0\rho}} \, e^{jk_0\rho} \, U(\varphi) \tag{58}$$

where

8

$$U(\varphi) = e^{-jk_0 D \sin\varphi} \sqrt{k_0 \sin\varphi} \sum_{m=-\infty}^{+\infty} E_m(-j)^m L_m(k_2\alpha, k_3\alpha) \sum_{n=-\infty}^{+\infty} \exp\left[j\frac{2\pi n}{d}A\right] \cdot$$

$$\cdot \frac{B_n^{(0)}(k_n(\varphi))}{\left(k_2^2 - k_n^2(\varphi)\right)^{1/4}} \exp\left[jD\left(k_2^2 - k_n^2(\varphi)\right)^{1/2} + jm\vartheta(k_n(\varphi))\right] \tag{59}$$

and

$$k_n(\varphi) = k_0 \cos\varphi - \frac{2\pi n}{d} \tag{60}$$

As far as the truncation of the infinite series appearing in (59) is concerned, similar arguments as for the truncation of the matrix equation (49) hold.

NUMERICAL RESULTS AND DISCUSSION

Based on the preceding analysis, numerical results for the scattering amplitude $|U(\varphi)|$ (plotted against the observation angle φ) have been obtained to examine the dependence of the scattered field on various parameters of the problem. The parameters varied are the roughness parameter h/d (surface height) and $k_0 d$ (spatial period), the thickness of the upper layer $k_0 b$, the normalized horizontal position of the scatterer A/d, the angle of incidence θ_i and the electric parameters of the ground and the scatterer. The frequency has been taken at 50 MHz and the normalized depth of the scatterer has been assumed to be $k_0 D = 8$, corresponding to a realistic depth (about 7 m) of possible buried scatterers.

First, the convergence of the solution has been verified by varying the truncation size N for the expansion of the incident field and the Green function in terms of Floquet waves, as well as the truncation size M for the eigenfunction expansion of the internal electric field. In most cases, values of N and M up to 5 and 10, respectively, have been found sufficient to achieve convergence. It has also been verified that M depends mainly on the characteristics of the scatterer, while N depends mainly on the characteristics of the profile, namely h/d and $k_0 d$. For large conductivities of the ground layers and / or large h/d values, a truncation size N up to 15 may be required. For the values of $k_0 d$ considered, the convergence region of the solution with respect to h/d is narrower than that encountered in the corresponding case of a one-layer ground [2]. This is due to the ill-conditioning of the method employed to treat scattering by the sinusoidal interface in combination with the existence of possible guided leaky waves even for shallower corrugations than in the one-layer case. Further on, the validity of the solution has been tested in the limit $h \rightarrow 0$, where the numerical results compare very well to those for the corresponding problem with a planar ground surface [9].

From the numerical results obtained, it seems that the factors influencing most the scattered field pattern are the conductivities of the two ground layers and the position of the cylindrical scatterer with respect to the dips and lifts of the sinusoidal surface. It has been observed that the scattered wave tends to emerge following the shortest path inside the ground, a quite reasonable effect which appears more clearly when the conductivity of the crust is large. Numerical results obtained for various values of the electric parameters of the scatterer, relatively close to those of the ground, (e.g. $\varepsilon_3 = 4$, $\sigma_3 = 0,01$) have been found to yield scattering patterns identical in shape to those of the hollow scatterer, though of somewhat smaller magnitude. The situation is different when the parameters of the scatterer differ by orders of magnitude from those of the ground, as in the case of underground water streams (ε_3

$= 80$, $\sigma_3 = 4$). In this case, the scattering pattern also closely resembles that of a hollow scatterer (though it appears somewhat suppressed for large observation angles, i.e. above 130° or so) but the scattering amplitude is about 2,5 times larger. This could be useful in detecting underground water pipes or streams in desert areas.
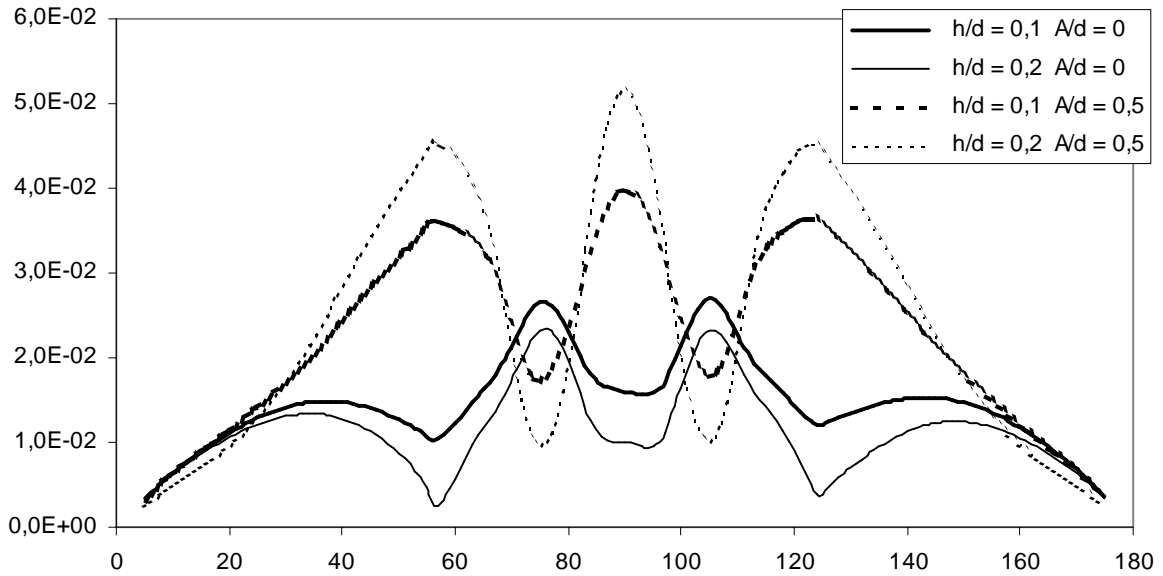
FIGURE 2. Variation of $|U(\varphi)|$ with h/d and A/d. The other parameters of the problem are $\theta_i = 40°$, $\varepsilon_1 = 4$, $\sigma_1 = 0,0001$, $\varepsilon_2 = 4$, $\sigma_2 = 0,001$, $\varepsilon_3 = 1$, $\sigma_3 = 0$, $k_0 b = 2$, $k_0 \alpha = 0,5$, $k_0 d = 4$.
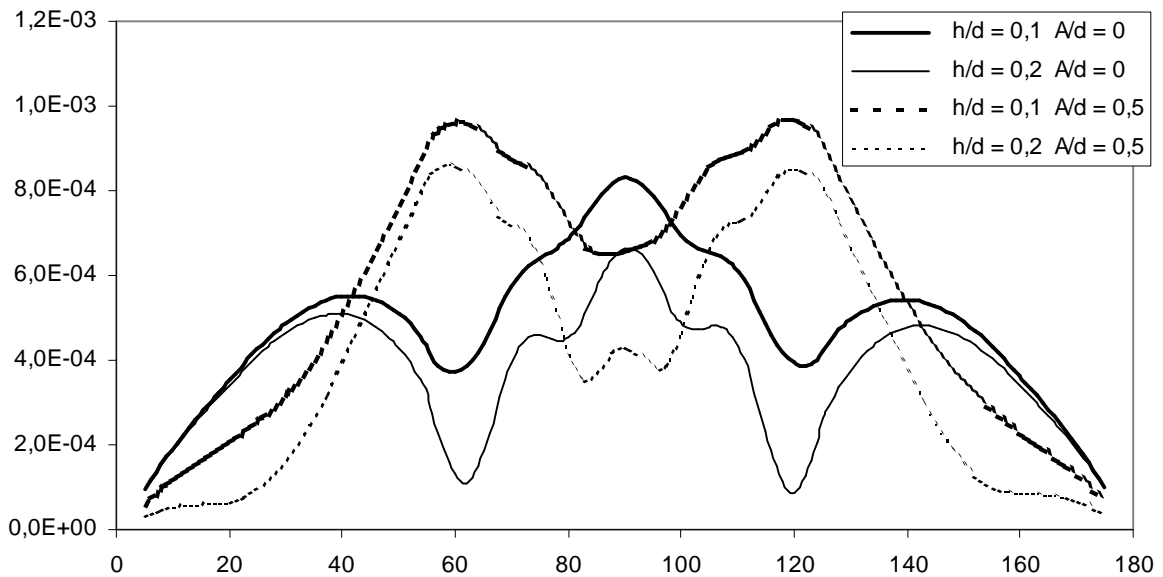
FIGURE 3. Same as in Fig. 2 but for $\sigma_1 = 0,01$.

The magnitude and shape of the scattered field are mainly determined by the effective depth of the scatterer, which depends on $k_0 D$, but also on $k_0 b$, σ_1 and σ_2 and its normalized horizontal position A/d. This is shown in Figs 2 to 5. Effective depth here means the degree of attenuation undergone by the incident filed on its way to the scatterer; in this sense, the effective depth of the scatterer tends to increase as σ_1 and/or $k_0 b$ increases (since the upper layer conductivity σ_1 in all practical cases is larger than σ_2).

10

When σ_1 is small (see Fig. 2), many lobes are observed, while the main part of the scattered energy is concentrated around the $\varphi = 90°$ direction. For larger values of σ_1 (see Figs 3 and 4), less lobes are observed. For comparable values of k_0b and k_0d corresponding to realistic situations, the direction of the main scattered lobes depends on whether the scatterer is located below a lift or a dip of the sinusoidal interface. When the scatterer is located right below ($A/d = 0$) or near ($A/d = 0,8$) a dip, the shortest path of emergence from the ground is along the $\varphi = 90°$ direction. When the scatterer is located right below ($A/d = 0,5$) or near ($A/d = 0,4$) a lift, two paths of emergence are favored, and therefore two lobes symmetrical with respect to $\varphi = 90°$ are observed.
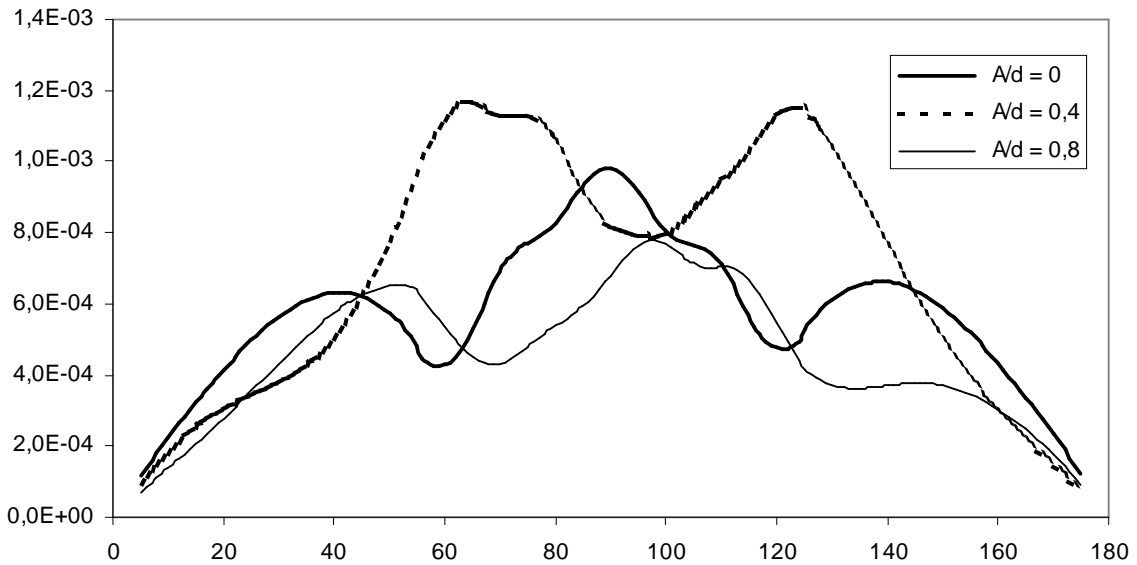
FIGURE 4. Variation of $|U(\varphi)|$ with A/d, where $h/d = 0,1$, $\theta_i = 20°$, $\varepsilon_1 = 4$, $\sigma_1 = 0,0001$, $\varepsilon_2 = 4$, $\sigma_2 = 0,001$, $\varepsilon_3 = 1$, $\sigma_3 = 0$, $k_0b = 2$, $k_0\alpha = 0,5$, $k_0d = 4$.
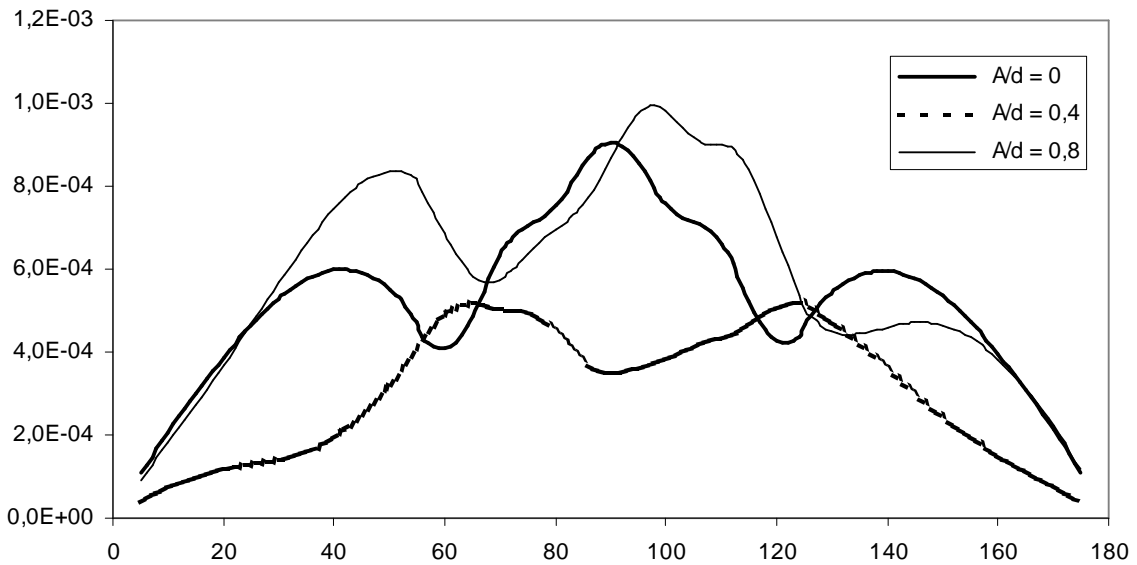
FIGURE 5. Same as in Fig. 4 but for $\theta_i = 50°$.

The dependence of the scattered field on k_0b , i.e. the surface layer thickness, is shown in

Fig. 6. Larger values of k_0b result in a severe decrease of the scattering amplitude, with the shape of the radiation pattern remaining more or less unchanged; this, of course, is to be attributed to the attenuation of the incident as well the scattered wave by the lossy layer.
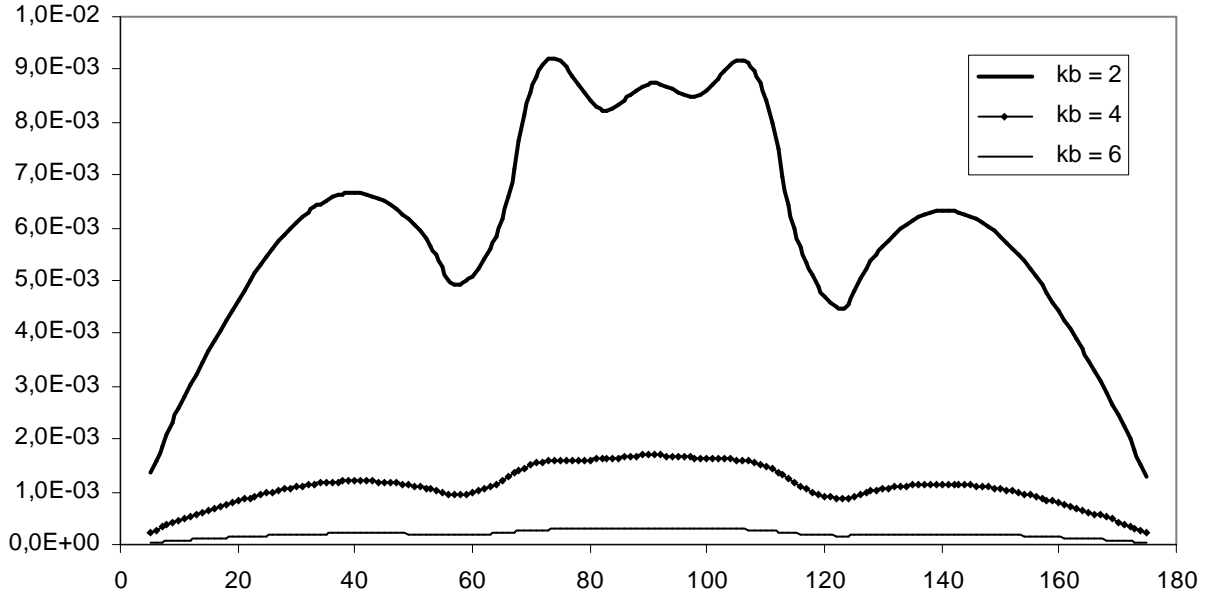
FIGURE 6. Variation of $\left| U(\varphi) \right|$ with k_0b, where $h/d = 0{,}2$, $A/d = 0$, $\theta_i = 20°$, $\varepsilon_1 = 4$, $\sigma_1 = 0{,}01$, $\varepsilon_2 = 4$, $\sigma_2 = 0{,}001$, $\varepsilon_3 = 4$, $\sigma_3 = 0$, $k_0\alpha = 1$, $k_0d = 4$.

In Figs 7 and 8, the scattering amplitude is plotted for a large surface roughness parameter h/d and various values of θ_i . Upon comparison of the two figures, it seems that the main factor affecting the scattering pattern is not the incidence angle but the horizontal position of the scatterer; two or three dominant lobes are observed, corresponding to the scatterer's location below a lift ($A/d = 0{,}5$) or a dip ($A/d = 0$), while the angles of maximum (about 60° and 120°) in the first case become angles of minimum in the second one.
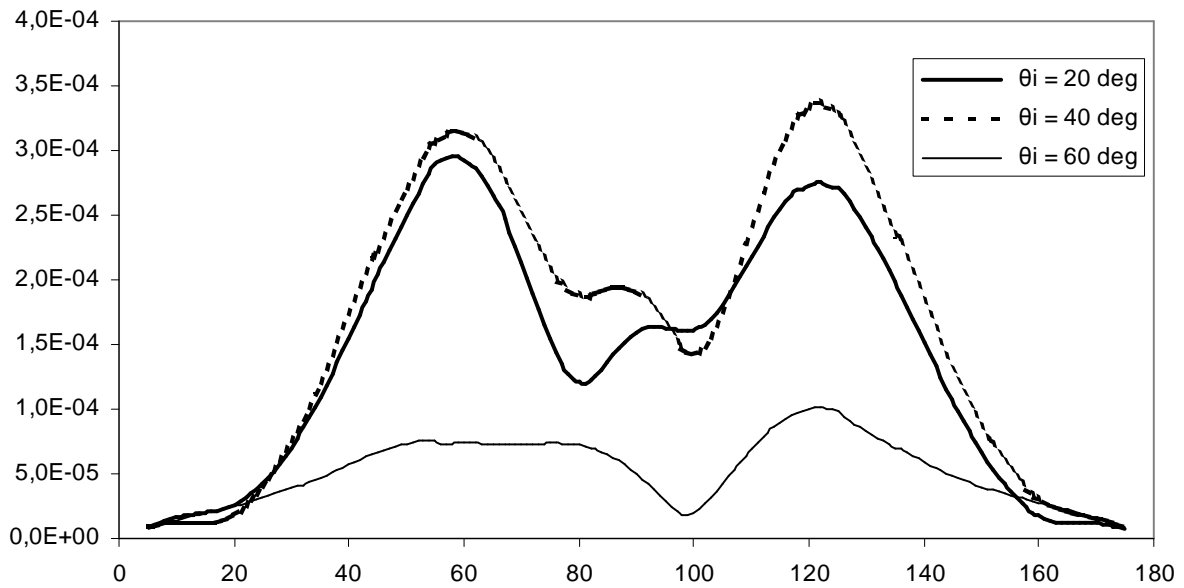
FIGURE 7. Variation of $\left| U(\varphi) \right|$ with θ_i , where $h/d = 0{,}3$, $A/d = 0{,}5$, $\varepsilon_1 = \varepsilon_2 = \varepsilon_3 = 4$, $\sigma_1 = \sigma_2 = 0{,}01$, $\sigma_3 = 1$, $k_0b = 2$, $k_0\alpha = 1$, $k_0d = 4$.
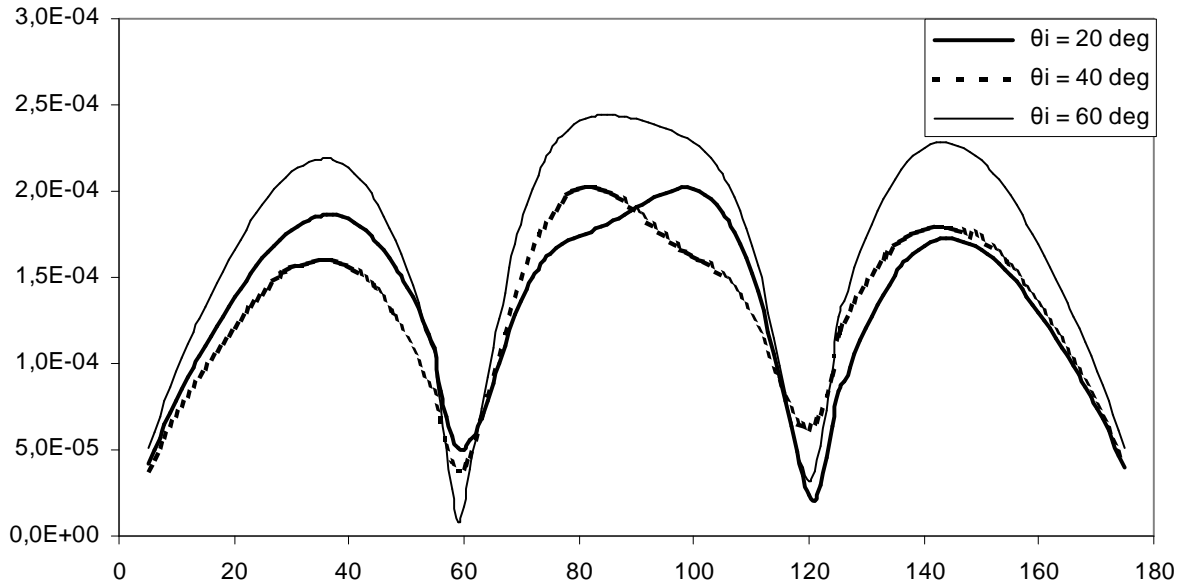
FIGURE 8. Same as in Fig. 7 but for $A/d = 0$.

Variation of the electrical radius $k_0\alpha$ of the scatterer leads to the results plotted in Fig. 9. As expected, increase of $k_0\alpha$ tends to significantly increase the scattered power and to narrow the main lobe of the scattering pattern.
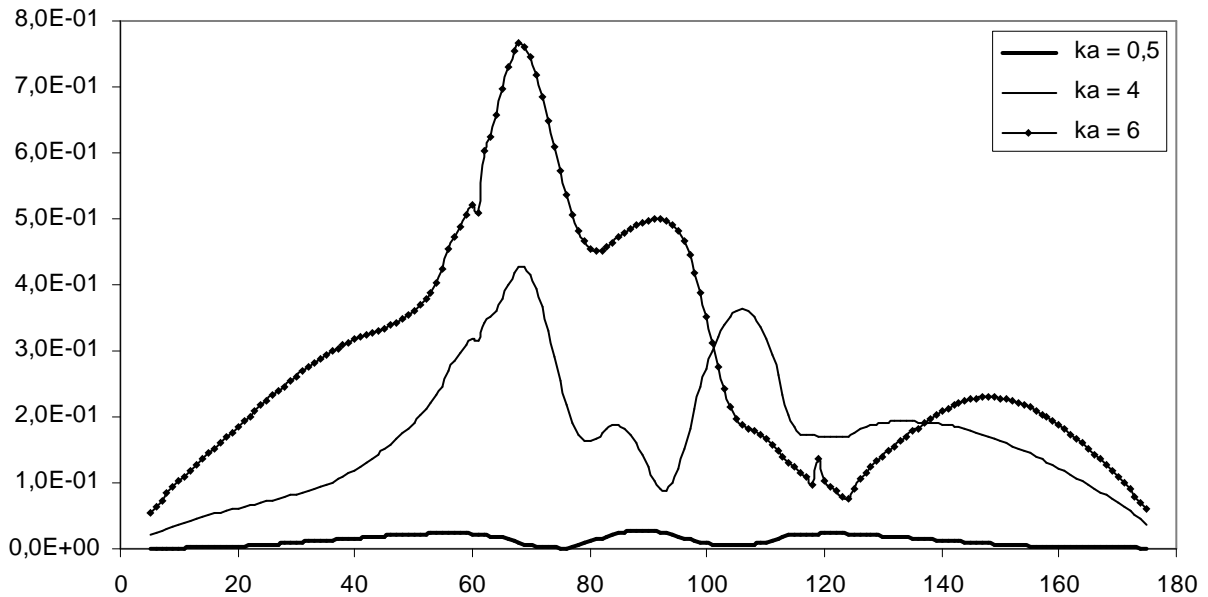
FIGURE 9. Variation of $|U(\varphi)|$ with $k_0\alpha$, where $h/d = 0,3$, $A/d = 0,5$, $\theta_i = 20°$, $\varepsilon_1 = \varepsilon_2 = 4$, $\sigma_1 = \sigma_2 = 0,001$, $\varepsilon_3 = 1$, $\sigma_3 = 0$, $k_0b = 2$, $k_0d = 4$.

In Figs 10 – 12, the influence of the surface roughness parameter h/d on the scattering amplitude is further examined for a relatively low conducting surface layer and various angles of incidence. It is seen that an increase of the corrugation depth affects to some extent the amplitude of the scattered field, but with a substantially unchanged shape of the scattering pattern; to state it in other words, it appears that the main difference is between plane and corrugated ground and not between grounds with different degrees of corrugation. This might be attributed to the effect of the preffered shortest path inside the ground, along with the small

13

number of nonevanescent Floquet modes (namely 2) corresponding to the value of k_0d under consideration. It is also seen that, for either relatively small or large incidence angles (20°, 60°) an increase in the roughness parameter tends to increase the scattering amplitude, while for an intermediate incidence angle (40°) the opposite trend is observed.
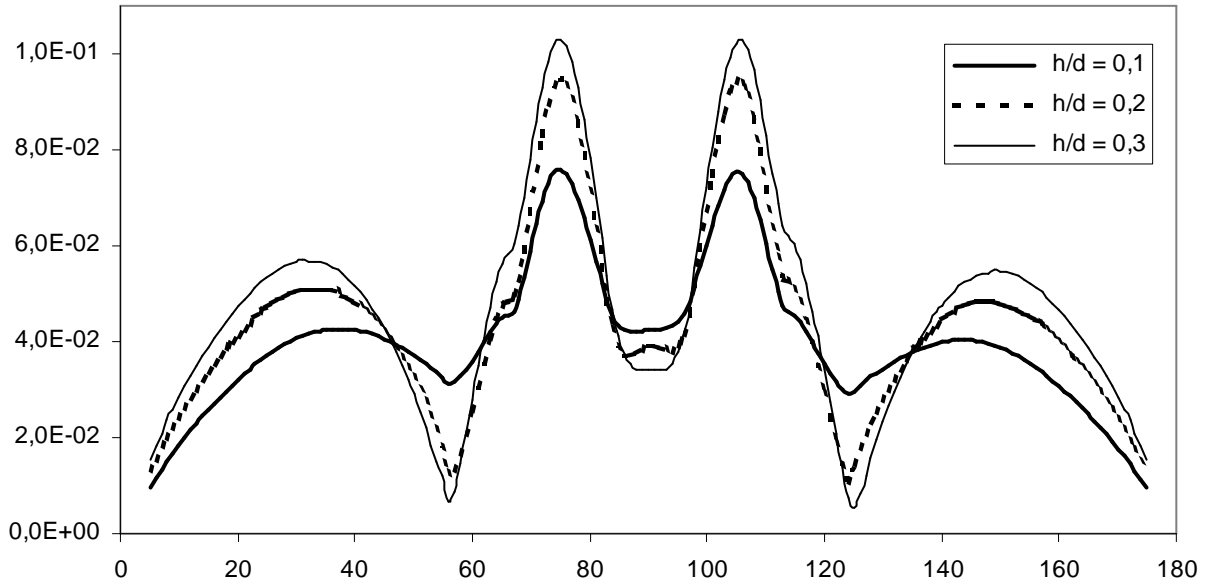
FIGURE 10. Variation of $|U(\varphi)|$ with h/d , where $A/d = 0$, $\theta_i = 20°$, $\varepsilon_1 = \varepsilon_2 = 4$, $\sigma_1 = 0,0005$, $\sigma_2 = 0,001$, $\varepsilon_3 = 1$, $\sigma_3 = 0$, $k_0b = 2$, $k_0\alpha = 0,5$, $k_0d = 4$.
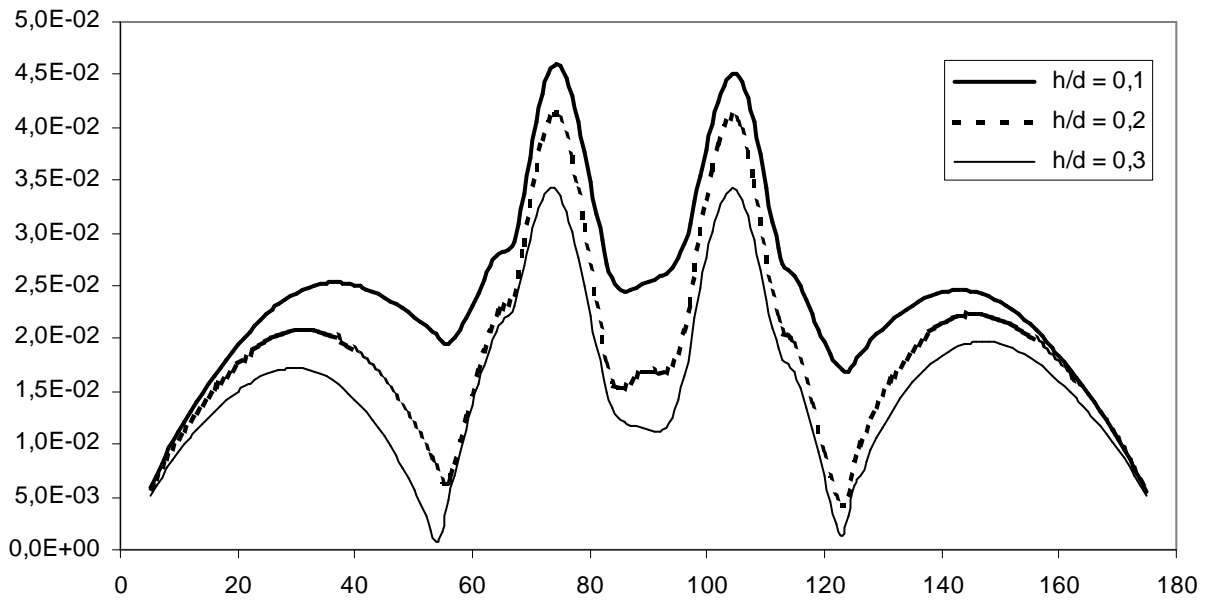
FIGURE 11. Same as in Fig. 10 but for $\theta_i = 40°$.

14
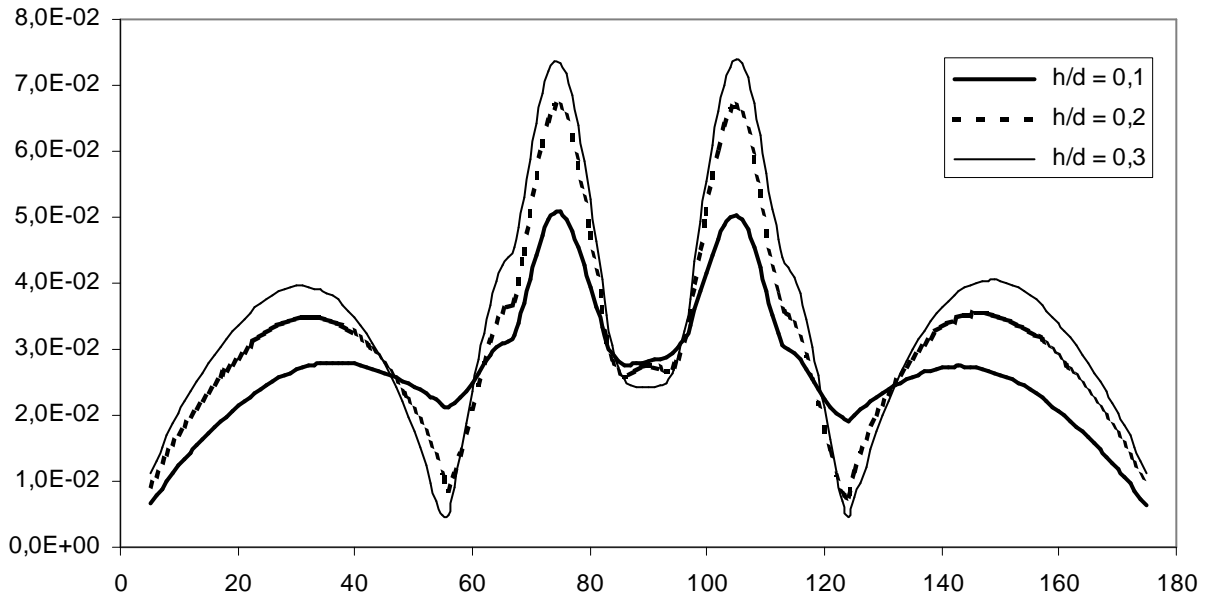
FIGURE 12. Same as in Fig. 10 but for $\theta_i = 60°$.

Figs 13-14 present analogous results, varying the surface roughness parameter h/d, for a surface layer of higher conductivity and two cases of spatial period k_0d. The higher conductivity of the surface layer tends to decrease the scattering amplitude and the number of lobes. It also seems that a larger value of k_0d, especially when combined with a large h/d parameter (i.e. for a large overall surface roughness), results in quite larger fluctuations in the scattering pattern.
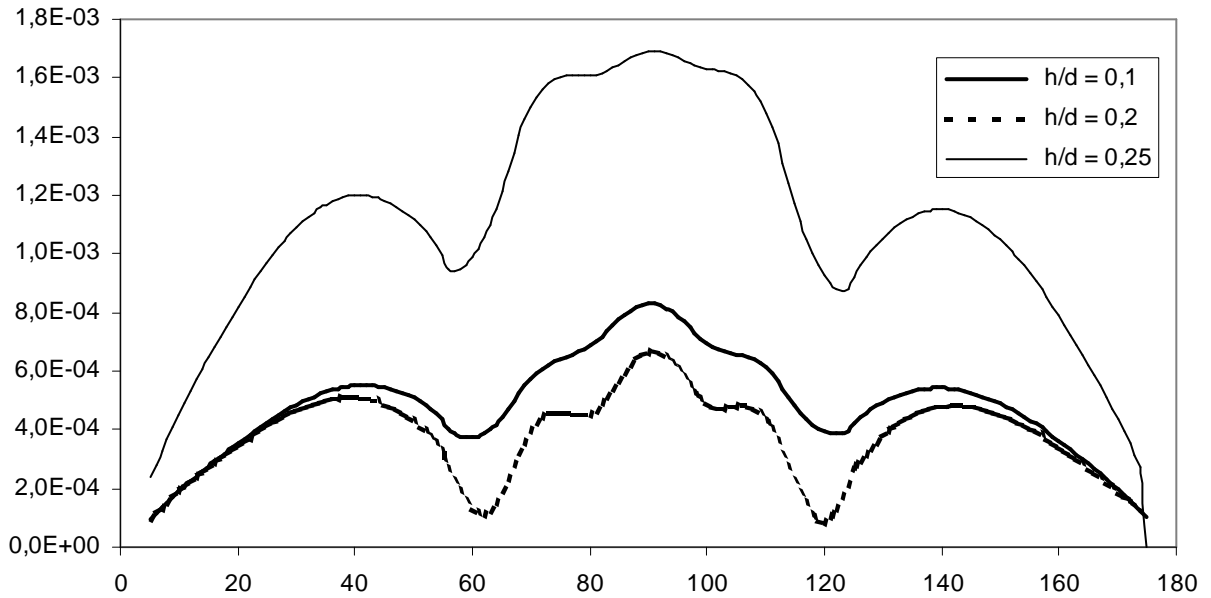
FIGURE 13. Variation of $|U(\varphi)|$ with h/d, where $A/d = 0$, $\theta_i = 60°$, $\varepsilon_1 = \varepsilon_2 = 4$, $\sigma_1 = 0,01$, $\sigma_2 = 0,001$, $\varepsilon_3 = 1$, $\sigma_3 = 0$, $k_0b = 2$, $k_0\alpha = 0,5$, $k_0d = 4$.

15
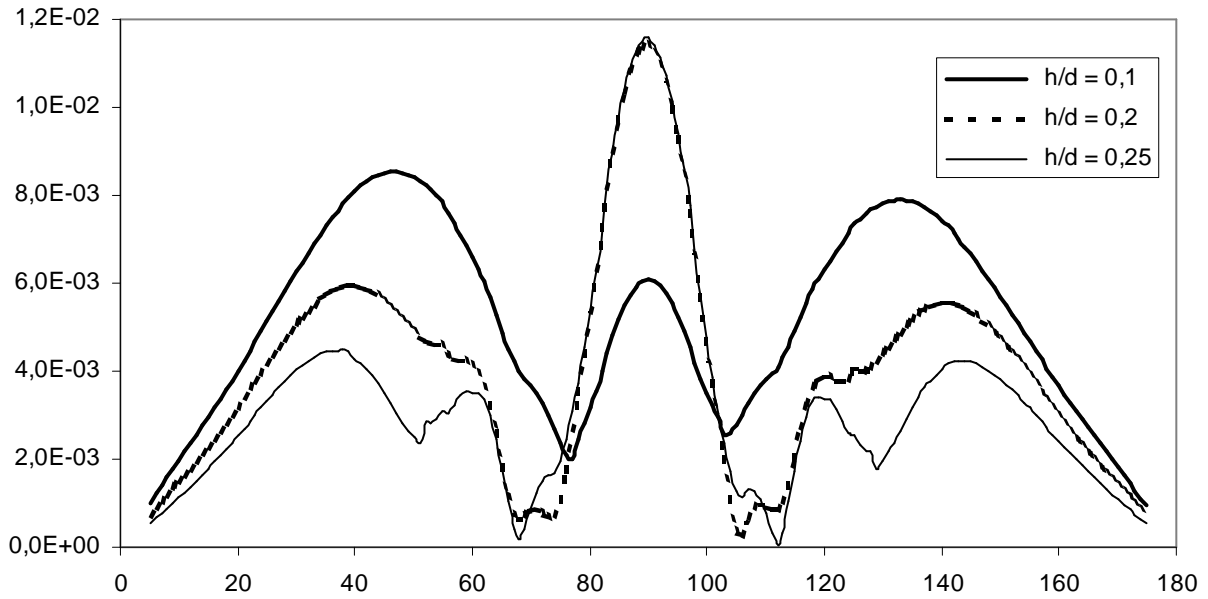
FIGURE 14. Same as in Fig. 13 but for $k_0 d$ = 8.

We note that in the opposite case of a small spatial period ($k_0 d = 2$), the corresponding results (not shown here) are very similar to those of [9] for the planar ground surface, with only one lobe; this may be explained based on the fact that the only significant Floquet mode reaching the scatterer (i.e. the only nonevanescent Floquet mode diffracted by the grating surface) is the zeroth-order one, easily verified to be along the direction given by Snell's law (as for a planar surface).

Finally, in Fig.15 results concerning underground water pipes are shown, which compared to the corresponding ones for a hollow scatterer (e.g. as in Fig. 13) are seen to yield patterns of similar shape, but significantly larger in magnitude.
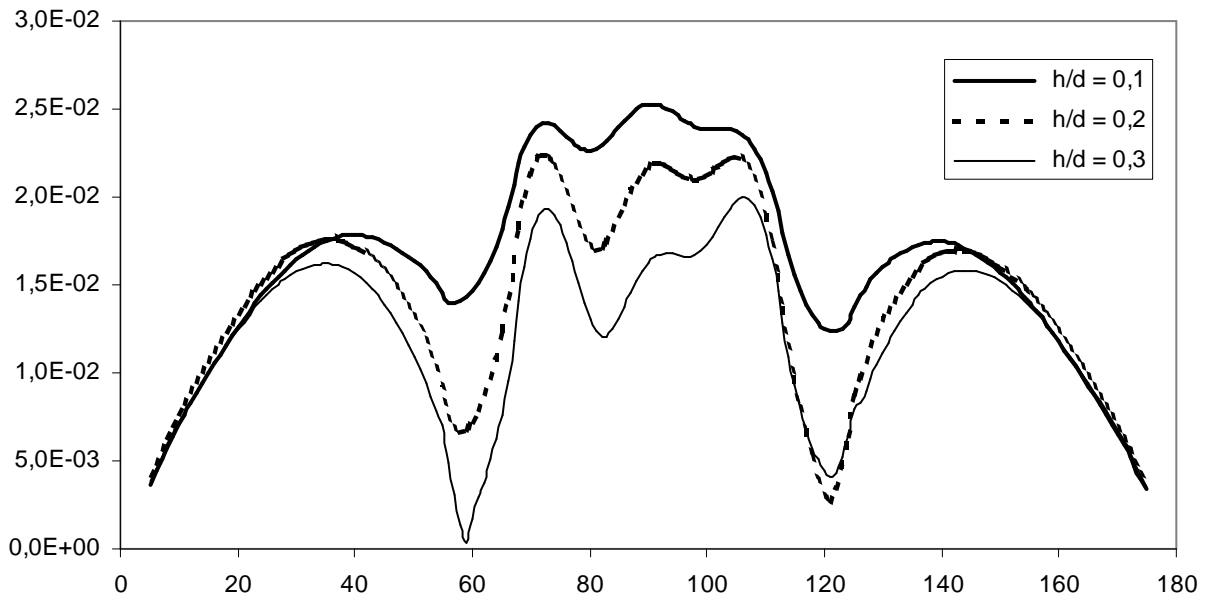
FIGURE 15. Variation of $|U(\varphi)|$ with h/d , where $A/d = 0$, $\theta_i = 20°$, $\varepsilon_1 = \varepsilon_2 = 4$, $\sigma_1 = 0,01$, $\sigma_2 = 0,001$, $\varepsilon_3 = 80$, $\sigma_3 = 4$, $k_0 b = 2$, $k_0 \alpha = 0,5$, $k_0 d = 4$.

CONCLUSIONS

The extended boundary condition approach has been employed to treat scattering of TE waves from a cylindrical scatterer buried inside a two-layer lossy ground with sinusoidal air-earth interface, allowing investigation for roughness depths substantially larger than perturbatively treated random roughness models. The numerical results obtained for the far-zone scattered field show that the factors mainly affecting the scattering amplitude are the conductivities of the ground layers, the horizontal position of the scatterer and its electric parameters.

REFERENCES

1. N. K. Uzunoglu and J. D. Kanellopoulos, "Scattering from underground tunnels", *J. Phys. A*, **15**, pp. 25-30 (1982).
2. P. G. Cottis and J. D. Kanellopoulos, "Scattering of electromagnetic waves from cylindrical inhomogeneities embedded inside a lossy medium with sinusoidal surface", *J. Electr. Waves Appl.* **6**, 445-458 (1992).
3. Y. Leviatan and Y. Meyouhas, "Analysis of electromagnetic scattering from buried cylinders using a multifilament current model", *Radio Sci.* **25**, 1231-1244 (1990).
4. K. Hongo and A. Hamamura, "Asymptotic solutions for the scattered field of a plane wave by a cylindrical obstacle buried in a dielectric half-space", *IEEE Trans. Antennas Propagat.* **AP-34**, 1306-1312 (1986).
5. A. Madrazo, J. R. Arias-Gonzalez and M. Nieto-Vesperinas, "Polarization effects in the scattering of electromagnetic waves by an object beneath a random rough surface", *Opt. Commun.* **162**, 91-98 (1999).
6. D. E. Lawrence and K. Sarabandi, "Electromagnetic scattering from a dielectric cylinder buried beneath a slightly rough surface", *IEEE Trans. Antennas Propagat.* **AP-50**, 1368-1376 (2002).
7. S. L. Chuang and J. A. Kong, "Scattering of waves from periodic surfaces", *Proc. IEEE* **69**, 1132-1144 (1981).
8. S. L. Chuang and J. A. Kong, "Wave scattering and guidance by dielectrtic waveguides with periodic surfaces", *J. Opt. Soc. Am.* **73**, 669-679 (1983).
9. J. D. Kanellopoulos, P. G. Cottis and P. G. Daniel, "Scattering of vertically polarized electromagnetic waves from infinite dielectric cylinders embedded in a lossy medium", *Int. J. Electronics* **59**, 423-433 (1985).